CRYSTAL GROWTH & DESIGN

Article

pubs.acs.org/crystal

Synthesis of Goethite α-FeOOH Particles by Air Oxidation of Ferrous Hydroxide $Fe(OH)_2$ Suspensions: Insight on the Formation Mechanism

Ezequiel R. Encina, Monica Distaso, Robin N. Klupp Taylor, and Wolfgang Peukert*

Institute of Particle Technology, Friedrich-Alexander University Erlangen-Nuremberg, Cauerstrasse 4, 91058 Erlangen, Germany

Supporting Information

ABSTRACT: Iron oxide and iron oxyhydroxide particles, particularly, the goethite α-FeOOH phase, are environmentally friendly materials and are used in various technological applications as adsorbents, precursors of Fe powders for magnetic recording media, and pigments. In this work, the formation process of α-FeOOH by air oxidation of $Fe(OH)_2$ suspensions has been studied. The effects of the air flow rate, as well as of the reactant concentration ratio, R (=$[(OH)^-]/[Fe(II)]$), on the reaction product were analyzed. It has been found that the morphology and the size of the α-FeOOH particles can be modified by means of the air flow rate. Furthermore, by performing a detailed microscopic analysis of the morphology of the initial, intermediate, and final reaction products, we have obtained evidence of epitaxial growth of α-FeOOH on the $Fe(OH)_2$substrate. It is suggested that the similarity between the anion arrangements in both phases facilitates this process. Based on these results, a pathway for the formation of α-FeOOH in highly alkaline medium is proposed in which the size and shape of the initial $Fe(OH)_2$ particles plays a significant role in the formation the α-FeOOH particles obtained upon completion of the oxidation process.

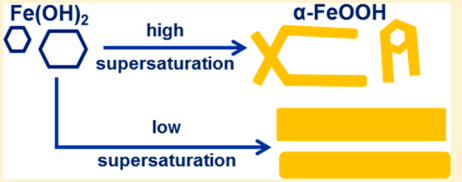

INTRODUCTION

Iron oxides and iron oxyhydroxides are materials that are widespread in nature and are of great industrial and scientific importance.[1] In particular, the α-FeOOH phase (goethite) is used in several technological applications such as adsorbents to remove toxic heavy metal ions and organic pollutants from wastewater,[2−5] precursors of Fe powders for magnetic recording media,[6−8] and pigments.[9,10] In all these applications, the size and shape distributions of the α-FeOOH particles are of paramount importance because they determine most of the physical properties of the particulate system. Therefore, knowledge of the particle formation mechanism is highly relevant in order to control the particle size and shape distributions by means of process parameters. The synthesis of α-FeOOH relies on the precipitation or oxidation/precipitation from Fe(III) or Fe(II) aqueous solutions, respectively.[11] In general, when Fe(III) salts, such as nitrate, are used as precursors, it has been established that in alkaline media the α-FeOOH formation follows a precipitation−dissolution−recrystallization mechanism with ferrihydrite as the intermediate metastable phase.[12−15] α-FeOOH can also be synthesized starting from Fe(II) salts, such as sulfate, by oxidation, generally accomplished by bubbling air into the aqueous solutions to induce the formation of Fe(III) species as precursors for the α-FeOOH formation.[16−19] In these cases, the pH is a key variable because it determines the reaction pathway and is usually determined by the reactant concentration ratio R (=$[(OH)^-]/[Fe(II)]$).[20,21] In the acidic regime, characterized by R < 2 values, it has been stated that α-FeOOH formation takes place through the formation of green rust, whose chemical formula has been suggested as $Fe^{II}_2Fe^{III}(OH)_7$,[1] as intermediate reaction product.[22−25] In the basic regime, characterized by R > 2 values, it has been reported that α-FeOOH formation occurs through a direct transformation of a ferrous hydroxide ($Fe(OH)_2$) phase.[26,27] In all the different possibilities mentioned above to prepare α-FeOOH, the particle size and shape distributions depend on the environmental conditions such as reactant concentrations, temperature, anion type, and additives.[28−36]

The procedure for preparing α-FeOOH by air oxidation of Fe(II) solutions in the basic regime has been known and employed for many years, particularly in the pigment industry, for large scale production.[1] However, to the best of our knowledge, there exists ongoing controversy regarding the α-FeOOH formation mechanism by this approach. Some authors have suggested that α-FeOOH nucleates homogeneously from the bulk of the liquid phase.[4,37] In contrast, other authors have suggested that α-FeOOH nucleates heterogeneously on the surface of $Fe(OH)_2$ crystals.[38,39] However, neither of the two hypotheses has been supported by strong experimental evidence. Therefore, understanding the α-FeOOH formation mechanism in the basic regime would be beneficial in order to develop synthetic strategies that permit greater control over the particle size and shape distributions.

In this work, the synthesis of α-FeOOH particles by air oxidation of $Fe(OH)_2$ suspensions has been studied. The effect of the air flow rate as well as of the above-defined reactant concentration ratio R on the reaction product has been analyzed. The α-FeOOH formation, in addition to the effect of

Received: August 8, 2014
Revised: October 21, 2014

   dx.doi.org/10.1021/cg501191h | Cryst. Growth Des. XXXX, XXX, XXX−XXX

the air flow rate on the evolving particle size and morphology, has been investigated by means of electron microscopy, XRD, and UV−vis measurements. Moreover, *in situ* Raman spectra have been acquired to further identify the iron oxide or oxyhydroxide phases formed during the course of the oxidation reaction. Microscopic analysis confirmed that a heterogeneous process is involved in the α-FeOOH nucleation and, combined with the other techniques used, enabled us to propose a plausible growth mechanism. We believe the results presented in this work constitute a timely contribution to a deeper understanding of the formation of α-FeOOH, a disperse system with widespread commercial relevance.

EXPERIMENTAL SECTION

Chemicals. Sodium hydroxide (NaOH, Carl Roth), and ferrous sulfate ($FeSO_4 \cdot 7H_2O$, Sigma-Aldrich), reagents of high purity grade, were used as received without further purification. Synthetic air (Linde, Synthetic Air) was employed as source of O_2. Aqueous solutions were prepared with ultrapure water (18.2 mΩ resistivity).

Apparatus. The reaction vessel employed was similar to that described by Kiyama.[40] In this case, a three-necked round-bottom flask, 500 mL in volume, was used. A glass tube with a glass frit (pore size 100−160 μm) at one end was adapted to fit the middle neck of the flask and used as gas distributor. N_2(g) or synthetic air at different air flow rates was passed through it accordingly. Temperature, pH, oxidation redox potential, dissolved oxygen, and *in situ* Raman spectra were measured to monitor the course of oxidation reaction by means of respective probes, which were introduced into the reaction vessel through the lateral flask necks.

Synthesis. In a typical experiment, 200 mL of NaOH solution of a given concentration was prepared in the reaction vessel and deoxygenated by bubbling N_2(g) for 2 h. Then, 150 mL of a deoxygenated $FeSO_4$ solution was added under continuous bubbling of N_2(g). The initial concentrations of the reactant solutions were adjusted in order to obtain, at the end of the mixing process, a 0.07 M $FeSO_4$ concentration and R (=$[(OH)^-]/[Fe(II)]$) values of 4, 5, and 6, respectively. Immediately after mixing the reactants, N_2(g) was switched to synthetic air in order to start the oxidation reaction. In all cases, the reaction temperature was 35 °C, and the suspension was stirred by using a magnetic stirrer (25 mm length, 12 mm diameter) at a rotation rate of 500 rpm.

***In Situ* Characterization of Reaction Mixtures.** The pH, redox potential, temperature, and oxygen content were determined *in situ* by using a multichannel Mettler Toledo transmitter unit (M800) equipped with a pH/redox probe (InPro4260i/SG/425 pH/redox) and an oxygen probe (InPro6860i/12/420). The determination of oxygen concentration in solution is based on quenching fluorescence resulting in the partial pressure of oxygen in equilibrium with the oxygen dissolved in solution. It was found that the time necessary to detect the dissolved oxygen in solution was 10 s, while the minimum detectable concentration of dissolved oxygen is 8 ppb. The Raman spectrometer was a Kaiser Optic instrument (RXN1-785) equipped with a diode laser with a wavelength of 785 nm and a stainless steel immersion probe equipped with a sapphire window. The investigated spectral range was 100−3425 cm^{-1} with a spectral resolution of 4 cm^{-1}; the power of the laser was fixed at 400 mW, while the acquisition time and the accumulation number were 5 s and 20, respectively.

UV−Vis Spectroscopy. The extinction spectra of the product suspensions at the end of oxidation process were measured using a Varian Cary 100 spectrophotometer with a cuvette of 1 cm optical path length. To obtain the extinction spectra, 10 μL was extracted from the reaction mixture and diluted 150 times with ultrapure water before each measurement.

XRD Characterization. The XRD instrument employed was a D8 Advance (Bruker AXS GmbH,Germany) using Cu Kα radiation (λ = 1.5406 Å). The diffractograms were obtained in the range 10−80° from powders of the particles. To obtain the respective powders, the suspensions containing the reaction products were washed through three cycles of centrifugation at 2683g (Andreas Hettich GmbH & Co.KG, Germany, Universal 320R), and the precipitated particles were dried in an oven overnight at 40 °C. The crystallite size was determined by applying the Scherrer equation to the (101) and (200) reflections; instrumental broadening was considered negligible and was not included in the analysis.

SEM and TEM Characterization. Aliquots of the reaction mixture were taken at different times; the as-obtained suspensions were deposited by spin-coating onto Si/SiO_2 substrates, and the particles were analyzed by SEM using an ULTRA 55 instrument (Carl Zeiss AG, Germany). The TEM and HRTEM images were obtained by using a CM 300 Ultra Twin microscope (Philips/FEI Company, The Netherlands) with the particles being deposited on a standard copper grid supported carbon film.

RESULTS AND DISCUSSION

All the experiments presented in this work were carried out following an identical procedure: 150 mL of a $FeSO_4$ solution was added, under continuous bubbling of N_2(g), to 200 mL of a NaOH solution of a given concentration determined by the R value. The formation of a white precipitate was observed after adding the first milliliter of the $FeSO_4$ solution, which gradually evolved to a pale green color suspension after completion of the mixing process. According to previous studies, this phenomenon is characteristic of $Fe(OH)_2$ formation.[41,42] Then, immediately after finishing the mixing of the solutions, the bubbling of N_2(g) was switched to synthetic air to start the oxidation reaction. It is important to note that the most important controlling parameters in this reaction are the reactant concentrations, the R value, the air flow rate, and the time of reaction. In the following, an investigation of the α-FeOOH formation mechanism is presented, which was carried out by a systematic variation of many of these controlling parameters. First, the influence of the air flow rate on the reaction product is investigated by keeping constant R (=$[(OH)^-]/[Fe(II)]$ = 6) and the Fe(II) concentration (0.07 M); then, the influence of R is studied while keeping the air flow rate (500 mL/min) and the Fe(II) concentration (0.07 M) constant.

***In Situ* Investigation of the Oxidation Reaction.** In order to monitor the course of oxidation reaction, the time evolution of the oxidation−reduction potential (ORP), as well as of the dissolved oxygen (DO), has been monitored. Figure 1a shows the time evolution of ORP (squares) and DO (triangles) for a particular experiment in which the air flow rate was fixed to 500 mL/min at R = 6. According to the Nernst equation, the initial decrease of the ORP values is consistent with an increase in the concentration of soluble Fe(II) species. The end of the oxidation process is characterized by a sharp increase in the ORP values. Therefore, the inflection point in the black curve (Figure 1a) after 57 min determines the end of the oxidation reaction, hereafter denoted as reaction time. The simultaneous measurement of DO (Figure 1, squares) shows that O_2 is detected after 54 min of reaction and that for longer times the amount of DO rapidly increases, reaching a plateau value of 170 mbar, which corresponds to the DO saturation value, after 70 min of reaction. Taken together, these two results unambiguously indicate that after 57 min of reaction all of the Fe(II), present as both soluble complexes and solid phases, has been oxidized to Fe(III) species by reaction with O_2.

This procedure to determine the reaction time was applied to all the experimental conditions used in this work. It is

dx.doi.org/10.1021/cg501191h | *Cryst. Growth Des.* XXXX, XXX, XXX−XXX

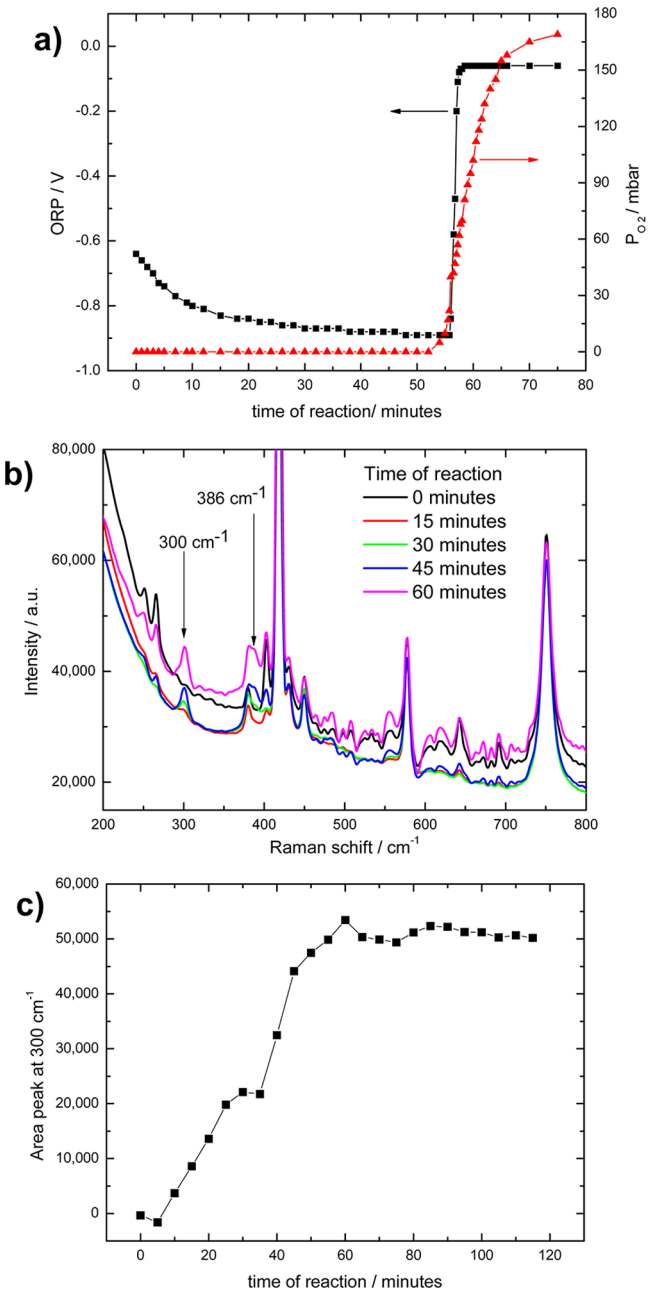

Figure 1. (a) Time evolution of the oxidation−reduction potential (ORP) (■) and dissolved oxygen (DO) (▲) with the course of oxidation reaction ([$FeSO_4$] = 0.07 M, R = 6, air flow rate = 500 mL/min). (b) Time evolution of the Raman spectra of the reaction mixture. The increase of intensity at Raman shift of 300 and 386 cm^{-1} coincides with the most intense Raman modes of α-FeOOH. (c) Area of the peak centered at 300 cm^{-1} vs time of reaction.

worthwhile to mention that under these experimental conditions the evolution of pH with the course of oxidation reaction shows a small decrease from an initial value of 12.8 to a final value, after completion of the reaction, of 12.4 in agreement with previous results.[20,24]

With the aim of identifying the different iron oxide or oxyhydroxide phases formed during the oxidation process, Raman spectra of the reaction system were measured *in situ*. Figure 1b shows the time evolution of the Raman spectra for the synthesis performed at R = 6 and 500 mL/min air flow rate. It has been found that the Raman signal intensity at 300 and 386 cm^{-1} increases with time of reaction. The Raman peak at 300 cm^{-1} and the shoulder at 386 cm^{-1} are attributed to α-FeOOH formation since the most intense Raman modes of this phase are centered precisely at 300 and 386 cm^{-1}.[43,44] Importantly, peaks that could be attributed to other iron oxide or oxyhydroxide phases are not observed providing further evidence for the direct transformation of $Fe(OH)_2$ to α-FeOOH. The main other visible peaks in the Raman spectra might be attributed to the excitation of different modes: the peaks at 418 and 450 cm^{-1} would be attributed to symmetric bending of SO_4^{2-} ions, while the peaks at 577 and 642 cm^{-1} would be attributed to antisymmetric bending of SO_4^{2-} ions, and the peak at 747 cm^{-1} might be associated with librational modes of water.[45] As will be discussed below, initial $Fe(OH)_2$ particles dissolve and are converted to α-FeOOH particles with the advance of oxidation reaction. In turn, during the experiments, air is continuously bubbling into the system. Therefore, the experimental conditions and the process that takes place during the oxidation reaction lead to a high inhomogeneity of the system. Because the probe employed to acquire the Raman spectra was immersed into the bulk of the reaction system, the nonlinear variation in the background of the spectra over time may be attributed in part to the fact that different amounts of material are sensed in different experiments. In addition, the area of the peak centered at 300 cm^{-1} can be estimated to be proportional to the amount of α-FeOOH formed. This parameter is plotted against time of reaction in Figure 1c. The plateau reached after 60 min confirms that α-FeOOH is no longer formed after that time, which is in full agreement with the ORP and DO measurements (Figure 1a).

Influence of the Air Flow Rate on the Size and Shape Distribution of the Reaction Product. The dependence of reaction time, determined by ORP measurements, on the air flow rate for R = 6 is shown in Figure 2. The reaction time decays exponentially as the air flow rate is increased, confirming a higher O_2 mass transfer from the gas to the liquid phase leading to a change of the homogeneous and heterogeneous oxidation rates. A higher amount of O_2 transferred into the solution will increase the oxidation rate of Fe(II) to Fe(III), the

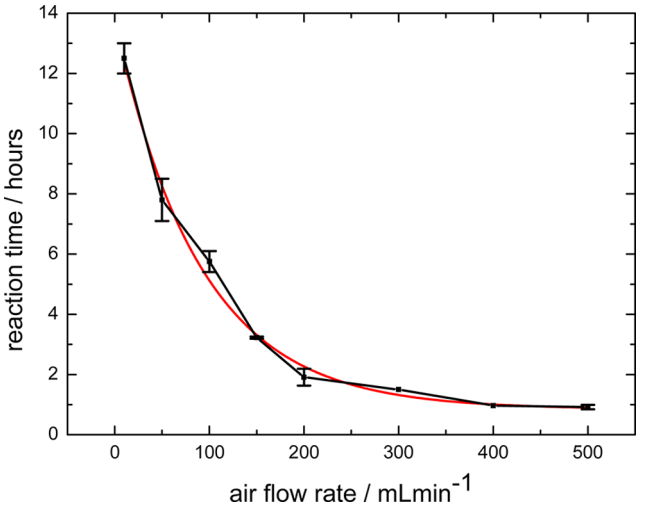

Figure 2. Dependence of the reaction time on the air flow rate ([$FeSO_4$] = 0.07 M, R = 6).The red curve describes the fit of the experimental data to an exponential decay curve.

dx.doi.org/10.1021/cg501191h | *Cryst. Growth Des.* XXXX, XXX, XXX−XXX

resulting increase in the α-FeOOH precursors concentration having an impact on the respective nucleation and growth process, leading to variation in the size and morphology of the particles produced.

We confirmed this influence through XRD measurements of powders produced under the same conditions as those in Figure 2. As shown in Figure 3, in all cases the measured peaks

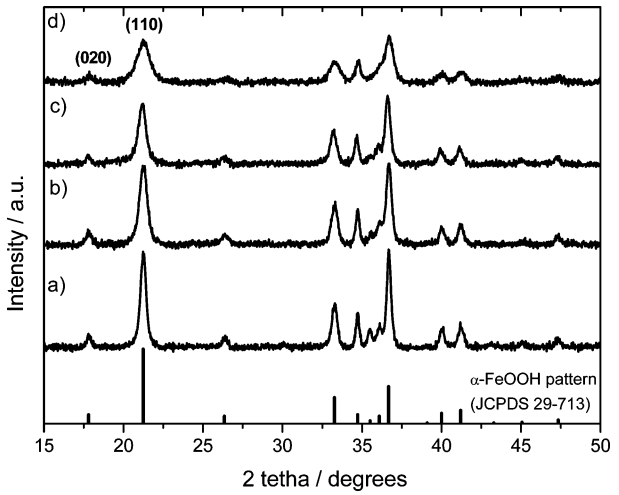

Figure 3. XRD patterns of the powders of α-FeOOH particles obtained at different air flow rate: (a) 10, (b) 50, (c) 100, and (d) 500 mL/min ($[FeSO_4]$ = 0.07 M, R = 6). The α-FeOOH reference XRD pattern (JCPDS 29-713) is also shown in the lower part of the figure. The patterns have been arbitrarily shifted in the y-axis.

match the α-FeOOH standard pattern (JCPDS 29-713), while diffraction peaks that could be attributed to other iron oxide or oxyhydroxide phases are not observed.

Synthetic α-FeOOH crystals usually exhibit needle shapes with the axis of elongation corresponding to the crystallographic c-axis.[1] Indeed, Lewis and Schwertmann stated that α-FeOOH particles synthesized from Fe(III) in alkaline media develop their final thickness along the crystallographic a-axis in the early stage of the reaction and subsequently they grow almost exclusively in width (along b-axis) and length (c-axis) until the ferrihydrite is completely transformed.[1S] The evolution of the XRD pattern with the time of reaction is not addressed in the current work; however this issue could be certainly studied in future works since it may provide valuable additional information on the growth process of α-FeOOH obtained by air oxidation of $Fe(OH)_2$ suspensions. Furthermore, such a study would help to clarify whehter the growth of α-FeOOH in alkaline media from Fe(II) as initial iron source exhibits the same features as the mechanism reported by Lewis and Schwertmann for the growth α-FeOOH in alkaline media with Fe(III) as initial iron source. XRD patterns presented in Figure 3 show a noticeable decrease in the full width at half-maximum of the (110) and (020) reflections as the air flow rate is decreased, which is attributed to an increase in the mean particle size. In particular for α-FeOOH, the mean coherence length perpendicular to the (020) planes, obtained by applying the Scherrer equation, gives a direct measure of the mean crystallite dimension in the b direction (MCD_b). Likewise, the mean crystallite dimension in the a direction (MCD_a) can be obtained from the mean coherence length perpendicular to the (110) plane corrected with respect to the angle between the (110) plane and the a axes.[26] Suitable reflections to evaluate the MCD_c (i.e., particle length) are not available in the XRD patterns presented in Figure 3, in agreement with previous studies.[46] The respective MCD_a and MCD_b values obtained for α-FeOOH particles synthesized at different air flow rates are shown in Table 1, clearly showing that the mean α-FeOOH crystallite size along the a and b directions decreases as the air flow rate is increased.

Table 1. Mean Crystallite Dimension in the a (MCD_a) and b (MCD_b) Directions for α-FeOOH Particles Obtained at Different Air Flow Rate Values

	air flow rate, mL min^{-1}			
	10	50	100	500
MCD_a, nm	17.6	12.6	12.6	7.8
MCD_b, nm	21.5	20.1	17.5	15.1

Further confirmation of the morphological changes implied by the XRD results was obtained using scanning electron microscopy (SEM). Figure 4 shows representative SEM images

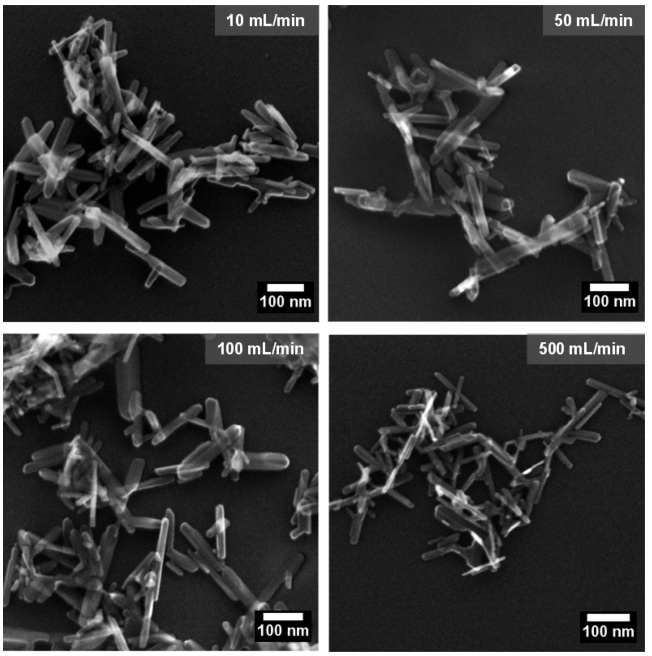

Figure 4. SEM images of the α-FeOOH particles obtained at different air flow rates ($[FeSO_4]$ = 0.07 M, R = 6).

of particles obtained at different air flow rate values in the range between 10 and 500 mL/min. In general, it can be observed that the obtained particles are elongated and exhibit a rod-like shape in agreement with the crystal habit of α-FeOOH. However, significant changes in the size and morphology of the α-FeOOH structures are also noticed as the air flow rate is increased from 10 to 500 mL/min. At relatively low air flow rate values (10 mL/min), mostly elongated particles are observed. At high air flow rate values (500 mL/min), the obtained particles are also elongated but often appear to be interconnected, leading to the appearance of hexagonal holes. Besides these changes in the morphology of the particles, SEM images also revealed that the mean size of the particles decreases as the air flow rate is increased.

In order to obtain quantitative information, statistical analysis of the images has been performed. The number density

dx.doi.org/10.1021/cg501191h | Cryst. Growth Des. XXXX, XXX, XXX−XXX

distribution of the length and width of the α-FeOOH particles obtained at different air flow rate values, which were obtained on the basis of counting two hundred particles in each case, are plotted in Figures S1 and S2 of Supporting Information, respectively. The mean values and standard deviations obtained from the fits of the number density distributions to log-normal distributions are plotted versus the air flow rate in Figure 5. It

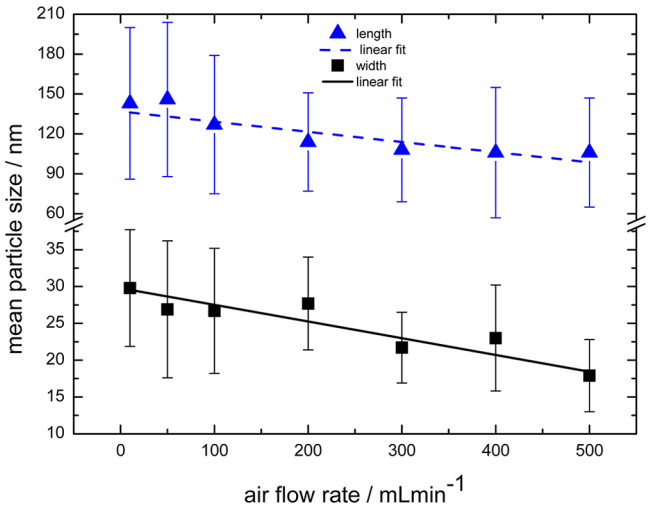

Figure 5. Dependence of the mean α-FeOOH particle length (▲) and width (■), along with its respective standard deviation, on the air flow rate ([$FeSO_4$] = 0.07 M, R = 6). Lines describe the fit of the data to linear functions.

can be observed that both the mean particle length and the mean particle width decrease almost linearly as the air flow rate is increased. This trend, at least for the particle width, is in agreement with the XRD results (Table 1). Nevertheless, due to the different slopes of the length and width variations and due to experimental scatter, less of a trend in aspect ratio with air flow rate is observed. The changing particle size and morphology with air flow rate can, as with the reaction time, be related to the increased O_2 mass transfer to the liquid phase at increasing air flow rates. This results in an acceleration of the formation of Fe(III) species generated leading to a higher supersaturation of the system and to a decrease in the critical nucleus size as well as to an increase in the nucleation rate.[47]

The effect of the air flow rate on the particle size is also manifested in the extinction spectra of the suspensions of the α-FeOOH particles, which are shown in Figure 6.

These spectra, whose features result from the contribution of different types of electronic transitions[48] and linear light scattering, resemble the spectra previously reported by Zhang et al.[49] for suspensions of α-FeOOH particles of different size. Slight but measurable shifts to longer wavelengths of the peaks in the UV region as well as an increase in the extinction intensity in the visible region are observed as the air flow rate employed in the synthesis is decreased. To relate these spectral changes to possible variations in the electronic structure of the produced materials, we determined the bandgap energy of the products using a Tauc–Mott analysis similar to that reported by Chernyshova et al.[50] Figure 7 shows the data of Figure 6 replotted as the squared product of E and absorbance A in dependence of the photon energy E. In order to correct the spectra for scattering, a linear baseline was subtracted, which was drawn by extrapolating a slope in the 700–800 nm range

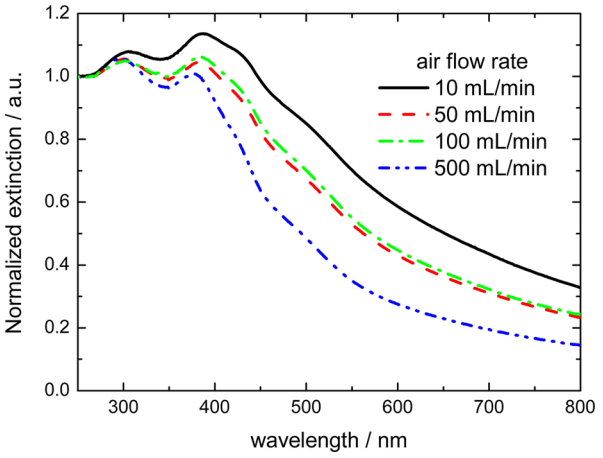

Figure 6. Extinction spectra of suspensions of the α-FeOOH particles obtained at different air flow rate values ([$FeSO_4$] = 0.07 M, R = 6).

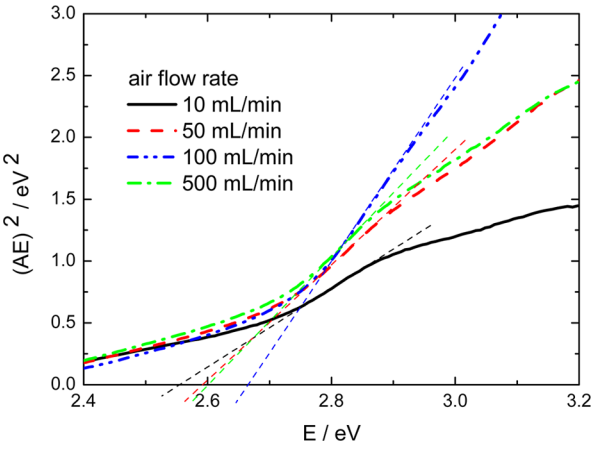

Figure 7. Tauc–Mott plots of the extinction spectra shown in Figure 6.

toward 200 nm, according to the approach applied in previous studies.[49,50] As stated by Chernyshova et al.,[50] this approach underestimates the contribution of scattering at short wavelengths λ, which increases as $1/\lambda^n$, n being the refractive index, but minimizes it in the absorption edge area.

The direct bandgap values of the α-FeOOH particles synthesized at different air flow rates, determined by extrapolating the linear section of plots in Figure 7 to the abscissa, are listed in Table 2. It is evident that the bandgap increases as the air flow rate is increased or, according to the SEM and XRD results, as the mean particle length and width are decreased.

In general for the iron (oxyhydr)oxides, and particularly for α-FeOOH, the size dependence of the bandgap is relevant for its reactivity in the environment as well as for technological applications such as lithium battery electrodes and solar energy devices.[49] In this regard, Chernyshova et al.[50] reported that for

Table 2. Bandgap, E_{gap}, Determined Based on Extinction Measurements of α-FeOOH Particle Suspensions Synthesized at Different Air Flow Rates

	air flow rate, mL min^{-1}			
	10	50	100	500
E_{gap}, eV	2.55	2.59	2.61	2.66

dx.doi.org/10.1021/cg501191h | Cryst. Growth Des. XXXX, XXX, XXX–XXX

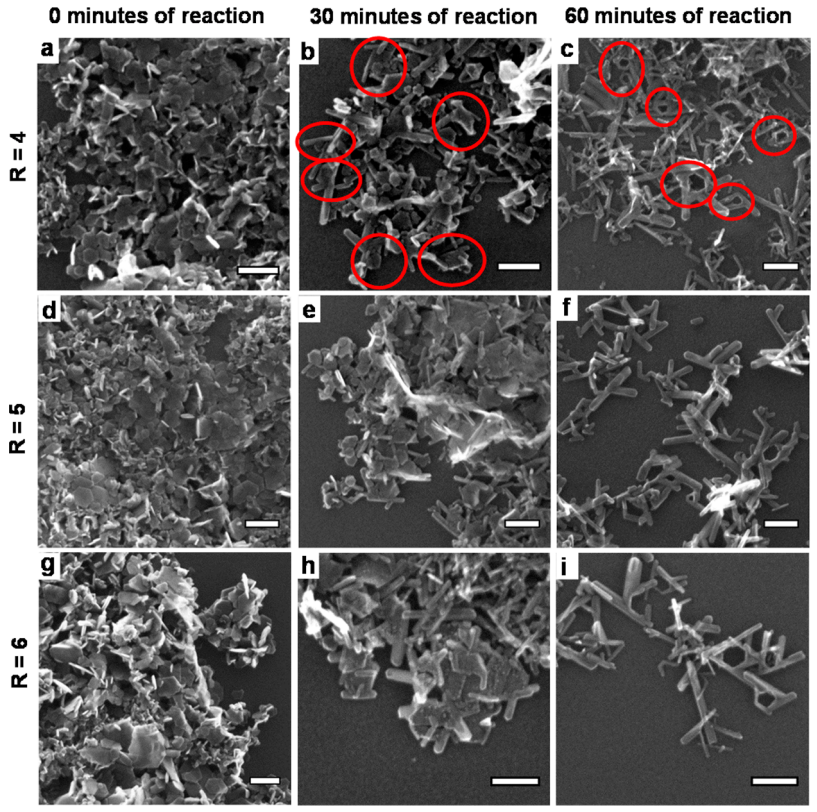

Figure 8. SEM images of the α-FeOOH particles formed at different times of reaction and different R values keeping all the other controlling parameters at constant values ($[FeSO_4]$ = 0.07 M, air flow rate = 500 mL/min). (a–c) R = 4; (d–f) R = 5; (g–i) R = 6. Scale bars correspond to 100 nm.

hematite particles the bandgap increases from 2.18 to 2.95 eV when the particle size is decreased from 120 to 7 nm. These authors found that the direct O 2p–Fe 3d charge transfer (CT) transitions dominate at the absorption edge of this oxide. Accordingly, the CT origin of the gap allows the attribution of the observed bandgap widening with decreasing particle size to weakening of the Fe 3d–O 2p hybridization. In addition, the lower overlap of the Fe 3d and the O 2p orbitals in smaller hematite particles probably stems from an increase in concentration of iron vacancies, which is accompanied by an increase in the a and c cell parameters and lattice disorder. Therefore, the decrease in the bandgap with increasing particle size is attributed to restoration of hematite lattice structure, which ultimately results in an increase in the O 2p–Fe 3d hybridization, stabilization of the valence band, and delocalization of valence electrons. In addition, they argued that this interpretation can be also extended α-FeOOH nanorods.[50] While in our case we cannot rule out some influence of the particle morphology on linear light scattering, which superimposes the effect of optical absorption, the large differences in the UV region point strongly to the fact that the air flow rate provides a simple means to adjust the electronic properties of the produced material.

Influence of *R* on the Size and Shape Distribution of the Reaction Product. It is well-known that the value of the parameter R (=$[(OH)^-]/[Fe(II)]$) plays a key role in the synthesis of iron oxyhydroxide particles by air oxidation of ferrous hydroxide suspensions. R determines relevant quantities, in particular the pH, and greatly affects the reaction pathway.[20] Therefore, the effects of R on the size and morphology of the initial, intermediate, and final reaction products are investigated in this section. It is important to mention that in the present study syntheses performed at R = 3 led at all flow rates to the formation of mixtures of α-FeOOH and magnetite (Fe_3O_4) (results not shown). In particular, the reaction time determined for R = 3 and an air flow rate of 500 mL/min is 50 min. However, for $R \geq 4$, α-FeOOH was the sole reaction product, consistent with the iron oxide phase distribution in the temperature vs R diagram reported by Kiyama.[40] In order to characterize the morphology and the size of the particles present at different stages of the oxidation reaction, 10 μL of the dispersion was extracted from the reaction vessel, deposited onto a silicon substrate by spin coating, and analyzed by SEM. Figure 8a,b,c shows representative SEM images of the particles formed after 0, 30, and 60 min of reaction, respectively, using conditions of R = 4, [Fe(II)] = 0.07 M, and an air flow rate of 500 mL/min. Under these experimental conditions, the reaction time was 52 min, while the initial pH value decreases from 12.6 to a final pH value of 12.3. Particles present before addition of air (0 min of reaction, Figure 8a) had a hexagonal platelet morphology in agreement with the $Fe(OH)_2$ crystal habit.[23] The platelet width was seen to range from 10 to 60 nm. It should be noted that $Fe(OH)_2$ is an extremely sensitive hydroxide, which is readily oxidized when it is exposed to atmospheric oxygen. Therefore, its direct morphological characterization is rather hard to accomplish.[51] However, the solvent is rapidly eliminated by our sample preparation procedure and thus any oxidation process of the initial $Fe(OH)_2$ particles should proceed via a topotactic mechanism, as already reported for the transformation from $Fe(OH)_2$ to δ-FeOOH.[52,53] Thus, whatever the chemical nature, it is assumed that the size and shape of the particles

dx.doi.org/10.1021/cg501191h | Cryst. Growth Des. XXXX, XXX, XXX–XXX

shown in Figure 8a represent the particle size and shape distribution of the $Fe(OH)_2$ particles suspended in the reaction system at 0 min of reaction. After 30 min of reaction, the SEM image (Figure 8b) indicates the presence of both hexagonal $Fe(OH)_2$ platelets as well as some elongated particles. It is important to note that the elongated particles appear very closely associated with or even connected to the hexagonal platelets, as indicated by the red circles.

This hints at a heterogeneous nucleation and growth of the α-FeOOH rods. After 60 min of reaction (Figure 8c), the particles observed consist mostly of structures with rod-like branches, while hexagonal platelets are no longer observed. The presence of hexagonal shaped holes between interconnected rod-like particles is also noted, as seen before in Figure 4. Figure 8, panels d–f and g–i, shows representative SEM images of the particles present in the reaction system at different times of reaction when the synthesis was performed at $R = 5$ and $R = 6$, respectively, while keeping constant all the other experimental variables (air flow rate 500 mL/min, $[Fe(II)] = 0.07$ M). At $R = 5$, the reaction time was 55 min, while the initial pH value decreases from 12.7 to a final pH value of 12.4. Regarding specifically the reaction time, the results obtained show that it increases as R increases. At first sight, this result may be rather unexpected taking into account that OH^- groups are consumed in the overall oxidation/hydrolysis reaction that leads to the α-FeOOH formation. However, it has been previously demonstrated that the solubility of O_2 decreases as the NaOH concentration increases,[54,55] a phenomenon that might explain the dependence experimentally found between R and the reaction time. In these cases, qualitatively the same changes are observed concerning the morphology of the particles formed at different times of reaction. Therefore, these results indicate that the R value within the range studied ($4 \leq R \leq 6$) does not substantially modify the size and morphology of the particles formed at the different stages of the oxidation reaction. Obviously, the initial $Fe(OH)_2$ particles are consumed and replaced by the formation of α-FeOOH particles. Furthermore, the morphological analysis of the initial, intermediate, and final particles suggests that the initial $Fe(OH)_2$ platelets act as template via a heterogeneous nucleation mechanism for the formation of α-FeOOH particles.

Figure 9a,b shows TEM images of the particles at 0 and 30 min of reaction for a synthesis performed at $R = 6$ and air flow rate 500 mL/min. These images can be directly correlated with the SEM images shown in Figure 8g,h, respectively. The particles obtained before the start of the oxidation (0 min of reaction) consist mostly of hexagonal platelets. After 30 min of reaction, the TEM image shows mixtures of elongated α-FeOOH particles attached to the surfaces of the hexagonal particles (Figure 9b). The region indicated with the black arrow in Figure 9b is shown with a higher magnification (under HRTEM conditions) in Figure 9c, where the lattice fringes corresponding to an elongated α-FeOOH particle, as well as the lattice fringes corresponding to an hexagonal $Fe(OH)_2$ particle, can be identified.

The fast Fourier transform analysis of the areas corresponding to the α-FeOOH (Figure 9d) and $Fe(OH)_2$ particle (Figure 9e), performed by means of the ImageJ software, indicates that in both cases the lattice spacing of planes has the same value, that is, 0.25 nm. This value is consistent with the spacing of the planes (101) in $Fe(OH)_2$.[51] Regarding α-FeOOH, the lattice spacing of 0.25 nm is consistent with the distance between planes (101), (040), and (111).[1] This continuity in the lattice

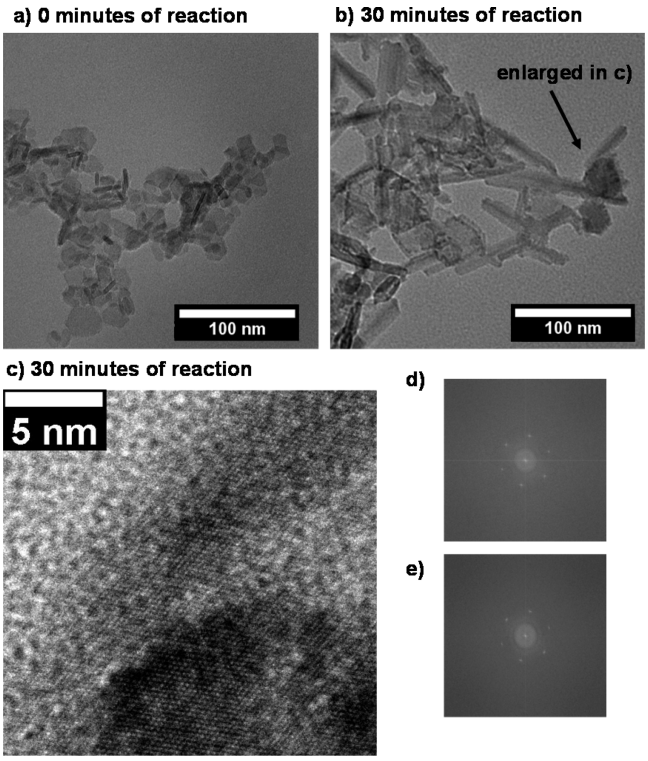

Figure 9. (a–c)TEM images of the α-FeOOH particles formed at different reaction stages ($[FeSO_4] = 0.07$ M, $R = 6$, air flow rate = 500 mL/min). (d, e) Fast Fourier transform analysis of the areas corresponding to the α-FeOOH (d) and $Fe(OH)_2$ particle (e).

spacing of planes between both particles provides further evidence that the formation mechanism α-FeOOH may occur through epitaxial growth on the $Fe(OH)_2$ substrate.

Discussion. Iron oxides and oxyhydroxides consist of arrays of Fe cations and O^{2-} and OH^- anions. As a consequence of the larger size of the anions in comparison with the cations, the crystal structures are governed by the arrangement of anions. In general, and particularly for $Fe(OH)_2$ and α-FeOOH, the crystal structures are based on hexagonal close packing of sheets of anions where the Fe cations fit into the octahedral interstices between the sheets. Thus, the main structural differences between the iron oxides are due to different arrangements of cations in the interstices between sheets of anions.[52] This relationship between the anion frameworks allows the topological conversion between different iron oxide phases. In fact, a topotactic conversion has been proposed for the transformation of $Fe(OH)_2$ to δ-FeOOH under conditions of rapid oxidation, for instance, when H_2O_2 is used as oxidizing agent.[56] However, the structures that can be identified in the HR-TEM image shown in Figure 9c, which correspond to the intermediate oxidation reaction products, suggest that α-FeOOH particles form through an epitaxial process, where the initial $Fe(OH)_2$ particles act as seeds for the heterogeneous nucleation of α-FeOOH. Based on this evidence, we propose that the formation of α-FeOOH particles by air oxidation of $Fe(OH)_2$ suspensions occurs by means of a dissolution–oxidation–recrystallization mechanism, in which the initial $Fe(OH)_2$ particles provide not only the source of Fe for the formation of the purely ferric phase but also the substrate for an epitaxial growth of α-FeOOH. The similarity between the arrangement of O^{2-} and OH^- anions in $Fe(OH)_2$ and α-

dx.doi.org/10.1021/cg501191h | Cryst. Growth Des. XXXX, XXX, XXX–XXX

FeOOH would facilitate the epitaxial growth of α-FeOOH over the $Fe(OH)_2$ substrate.

Misawa et al.[21] proposed that the formation of α-FeOOH by means of air oxidation of highly alkaline $Fe(OH)_2$ suspensions involves the dissolution of the hydroxide particles, followed by homogeneous oxidation of the $Fe(OH)_3^-$ complex to the neutral $Fe(OH)_3$ species, which then polymerizes, presumably by olation reaction, leading to an amorphous ferric oxyhydroxide phase $FeO_x(OH)_{3-2x}$, which rapidly converts to α-FeOOH. Indeed, it has been stated that due to the extensive atomic rearrangements required for aqueous ions to form any crystalline iron oxide or oxyhydroxide, these solids are in general not crystallized directly but are formed rather by a precipitation−dissolution−recrystallization mechanisms. A related consequence is that the homogeneous nucleation of crystalline phases is probably avoided.[57,58] The scheme suggested by Misawa et al.[21] resembles the mechanism proposed for the formation of α-FeOOH from Fe(III) sources in alkaline media. In these cases, it has been established that the metastable phase ferrihydrite, whose chemical formula may be expressed as $Fe_5O_8H{\cdot}H_2O$, initially forms as an intermediate hydrolysis product, which then dissolves to release soluble species of $Fe(OH)_4^-$ from which the less soluble α-FeOOH phase forms following by a dissolution−recrystallization mechanism.[11] It is worthwhile to note that the conversion time of ferrihydrite to α-FeOOH in alkaline solution at room temperature is on the order of days or even higher.[59,60] However, to the best of our knowledge, a conclusive characterization of the amorphous ferric oxyhydroxide phase $FeO_x(OH)_{3-2x}$ that should precede (following the Ostwald step rule) the homogeneous nucleation of α-FeOOH when it is synthesized by air oxidation of highly alkaline $Fe(OH)_2$ suspensions has not been reported in literature. Furthermore, in our experiments, the formation of intermediate less stable iron oxyhydroxide phases, such as ferrihydrite, have been not observed. The thermodynamic energy barrier, ΔG_c, for heterogeneous nucleation is smaller than that for homogeneous nucleation[47] and the rate of nucleation is proportional to $e^{-\Delta G_c/(k_B T)}$, that is, α-FeOOH forms more rapidly through the pathway with the lower energetic barrier. In summary, we propose that the formation of α-FeOOH proceeds by means of heterogeneous nucleation and growth on surface of the $Fe(OH)_2$ platelets.

The formation of the precursors for the α-FeOOH precipitation is determined by the oxidation process of Fe(II) to Fe(III) species as suggested by Misawa et al.[21] Furthermore, iron oxyhydroxide surfaces are known to catalyze the oxidation of adsorbed Fe(II) species.[61−64] For instance, Tamura et al.[65] has shown that the presence of α-FeOOH accelerates the oxidation rate of Fe(II). Moreover, based on a density functional theory study, Russell et al.[66] stated that the electron transfer to the oxygen molecule is greatly enhanced for Fe(II) complexes bound to α-FeOOH surfaces. Therefore, the heterogeneous oxidation of Fe(II) species might also play a significant role in the growth of α-FeOOH particles. In this context, and according to the experimental conditions employed in this work, the following main pathways for the oxidation of Fe(II) species are suggested: (a) homogeneous oxidation of $Fe(OH)_3^-$ species, fed by the dissolution of $Fe(OH)_2$ particles, to give mainly $Fe(OH)_3$ and $Fe(OH)_4^-$ soluble species; (b) heterogeneous oxidation of Fe(II) species adsorbed on the surface of already nucleated α-FeOOH particles.

Taking into account that at pH > 11 the largely predominant ferrous complex is $Fe(OH)_3^-$,[55] the oxidation rate equation can be described as[62]

$$-\mathrm{d}[\mathrm{Fe(II)}]/\mathrm{d}t = (k_3' + k_s'[\mathrm{Fe(III)}])[\mathrm{Fe(II)}] \quad (1)$$

where k_3' is the rate constant for the homogeneous reaction[67,68] and k_s' is the rate constant for the heterogeneous reaction.[65] As far as we know, experimentally determined values of k_3' are not reported in literature; only Millero[67] suggested an estimated value of 1×10^8 min^{-1}, while experimentally determined values of k_s' were reported by Tamura et al.[65] The autocatalytic rate law (eq 1) clearly shows that the contribution of the heterogeneous reaction to the overall reaction rate is dependent on Fe(III) concentration and, accordingly, its contribution increases with the time of reaction. Based on eq 1, it was possible, after making several assumptions, to integrate an expression that accounts for the variation of Fe(II) concentration on the time of reaction (for a detailed description, see Supporting Information). By means of a fitting procedure, in which the k_s' values reported by Tamura et al.[65] were employed, a value of $k_3' = 8.4 \times 10^8$ min^{-1} was obtained for the oxidation rate of $Fe(OH)_3^-$, similar to the value suggested by Millero. The obtained value is larger than the values reported for the oxidation rate constant of $Fe(OH)_{2(aq)}$ (4.3×10^5 min^{-1}), $Fe(OH)^-$ (1.7 min^{-1}), and Fe^{2+} (6×10^{-5} min^{-1}) species, which is in agreement with the general trend where hydrolyzed ferrous iron species are more readily oxidized than nonhydrolyzed ferrous species.[68] Lastly, it is expected that the heterogeneous reaction has more significant influence in the crystal growth process than in the nucleation stages. However, deep comprehension of the effects of these two different paths for the oxidation of Fe(II) on the α-FeOOH particle size distribution is an issue that remains elusive and could be the subject of further studies.

The experimental results presented above along with the previous analysis allow us to propose a formation pathway for α-FeOOH formation by air oxidation of $Fe(OH)_2$ suspensions. Initially, the homogeneous oxidation of $Fe(OH)_3^-$ species leads to the formation of $Fe(OH)_4^-$, which is the precursor for the epitaxial growth of α-FeOOH on the surface of the hexagonal $Fe(OH)_2$ platelets. Under conditions of high air flow rate, large concentrations of $Fe(OH)_4^-$ species should form near the $Fe(OH)_2$ particles, which lead to a high local supersaturation and thus to epitaxial growth of α-FeOOH on all sides of the hexagonal platelets. The observation of epitaxial growth of α-FeOOH only on the sides of the hexagonal $Fe(OH)_2$ platelets might be attributed to different reasons: a larger lattice mismatch between different facets of the $Fe(OH)_2$ platelet and α-FeOOH, higher kinetic or thermodynamic stability of some facets of the $Fe(OH)_2$ platelet, or higher affinity of adsorbed SO_4^{2-} anions for some facets of the $Fe(OH)_2$ platelet. Further studies are needed in order to clarify this issue. Next, the already nucleated structures grow with the advance of the oxidation reaction until they coalescence at the vertices of the original hexagonal platelets. Considering the dissolution of the $Fe(OH)_2$, which must proceed with the oxidation reaction, the frequent appearance of hexagonal holes in the produced particles at high air flow rates (see Figures 4 and 8) can be explained. Under conditions of low air flow rate, the concentration of $Fe(OH)_4^-$ species is relatively low with lower supersaturations and, consequently, leads to a lower heterogeneous nucleation rate. Accordingly, the α-FeOOH nucleation may occur only on a few of the edges of the

dx.doi.org/10.1021/cg501191h | Cryst. Growth Des. XXXX, XXX, XXX−XXX

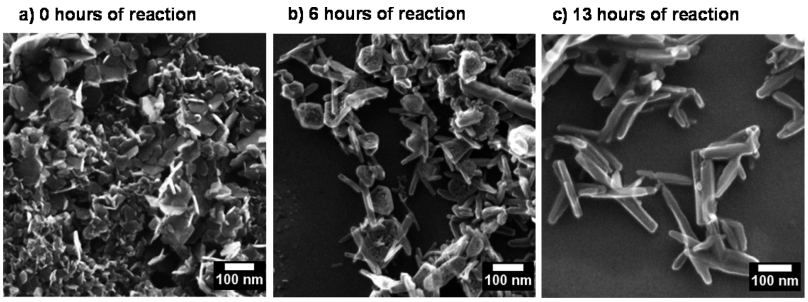

Figure 10. SEM images of the particles formed at different reaction stages ([$FeSO_4$] = 0.07 M, R = 6, air flow rate = 10 mL/min).

hexagonal $Fe(OH)_2$ platelets and result in isolated nanorod-like product particles (see Figure 4). This conclusion is backed up by Figure 10, which shows representative SEM images of particles obtained at different reaction times for R = 6 and an air flow rate = 10 mL/min. Before the start the oxidation reaction (Figure 10a), the particles exhibit mostly hexagonal shapes with sizes between 10 and 60 nm as noted previously. However, due to a the lower oxidation rate in this case, the precipitation of α-FeOOH takes place over a much longer period of time. After 6 h of reaction, a mixture of hexagonal and elongated particles is observed (Figure 10b). Similarly to the structures shown in Figure 8b,e,h, the elongated particles appear attached to the sides of the hexagonal platelets.

After completion of the reaction (Figure 10c), mostly elongated α-FeOOH particles are obtained, while branched structures with the hexagonal holes are rarely observed in contrast with the particles obtained at higher air flow rate values (Figure 8c,f,i). The above-described mechanism for α-FeOOH particle formation by air oxidation of $Fe(OH)_2$ suspensions as inferred by the present study is depicted schematically in Scheme 1. Lastly, it is important to note that Olowe and Génin[69] already studied the formation of α-FeOOH by air oxidation of $Fe(OH)_2$ suspensions based on Mössbauer spectroscopy measurements, under experimental conditions quite similar to those employed in the current work. By analyzing Mössbauer spectra obtained at different times of reaction, these authors found that the initial reaction product, after mixing the reactants, is $Fe(OH)_2$ and that its further oxidation leads to the formation of α-FeOOH, which takes place in at least two stages: the formation of its nucleus from a paramagnetic active ferric component (characterized as α'-FeOOH), whose proportion is always small and only detected at the initial stages of the oxidation reaction, followed by the growth of this nucleus. Importantly, the formation mechanism proposed by Olowe and Génin, based on Mössbauer spectroscopy measurements, is in full agreement with the mechanism proposed in the current work.

Scheme 1. Schematic Representation of the Pathway for the α-FeOOH Particle Formation by Air Oxidation of Ferrous Hydroxide $Fe(OH)_2$ Suspensions

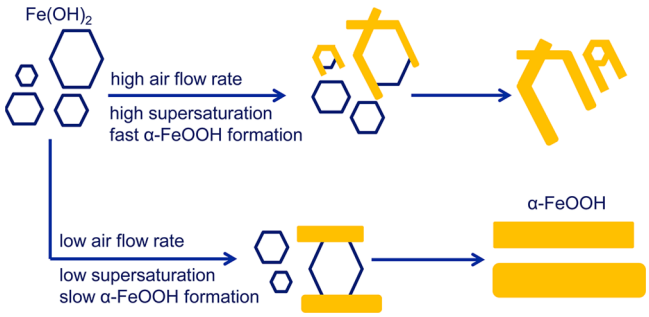

CONCLUSIONS

In this work, the synthesis of goethite α-FeOOH particles by air oxidation of ferrous hydroxide $Fe(OH)_2$ suspensions has been studied. We found that the air flow rate and consequently the O_2 mass transfer from the gas to the liquid phase has a remarkable effect on the size and morphology of the α-FeOOH particles. Particularly, it has been demonstrated that the mean length and mean width of the α-FeOOH particles decrease almost linearly as the air flow rate is increased. By means of careful SEM and TEM characterization of the initial, intermediate, and final reaction products, evidence of epitaxial growth of α-FeOOH on the edges of hexagonal $Fe(OH)_2$ platelets has been obtained for the first time. The heterogeneous nucleation of α-FeOOH on the $Fe(OH)_2$ substrate should be facilitated by the similarity between the anion arrangements in both phases. In summary, we propose a pathway for α-FeOOH formation in agreement with the experimental results. We believe that the greater understanding of the α-FeOOH formation process developed in this work will lead to the establishment of processes providing better control over particle morphology and size distribution, resulting in more effective α-FeOOH particles for a range of applications.

ASSOCIATED CONTENT

Supporting Information

Number density distribution of the length (larger dimension) and width (shorter dimension) of the α-FeOOH particles obtained at different air flow rate values and estimation of the oxidation rate constant k_3'. This material is available free of charge via the Internet at http://pubs.acs.org.

AUTHOR INFORMATION

Corresponding Author

*E-mail address: wolfgang.peukert@fau.de (W. Peukert) Tel: +49 9131 8529401- Fax: +49 9131 8529402.

Notes

The authors declare no competing financial interest.

ACKNOWLEDGMENTS

The authors acknowledge funding from the Deutsche Forschungsgemeinschaft (DFG) through the Cluster of Excellence Engineering of Advanced Materials and Lanxess for fruitful discussions and financial support.

REFERENCES

(1) Cornell, R. M.; Schwertmann, U. *The Iron Oxides: Structure, Properties, Reactions, Occurrence and Uses*; VCH: Weinheim, Germany, 1996.
(2) Waiman, C. V.; Avena, M. J.; Regazzoni, A. E.; Zanini, G. P. *J. Colloid Interface Sci.* **2013**, *394*, 485−489.
(3) Wang, Y.; Ma, J.; Chen, K. *Phys. Chem. Chem. Phys.* **2013**, *15*, 19415−19421.
(4) Wang, B.; Wu, H.; Yu, L.; Xu, R.; Lim, T.; Lou, X. *Adv. Mater.* **2012**, *24*, 1111−1116.
(5) Li, H.; Li, W.; Zhang, Y.; Wang, T.; Wang, B.; Xu, W.; Jiang, L.; Song, W.; Shu, C.; Wang, C. *J. Mater. Chem.* **2011**, *21*, 7878−7881.
(6) Pozas, R.; Ocana, M.; Puerto Morales, M.; Serna, C. J. *J. Colloid Interface Sci.* **2002**, *254*, 87−94.
(7) Nunez, N.; Puerto Morales, M.; Tartaj, P.; Serna, C. J. *J. Mater. Chem.* **2000**, *10*, 2561−2565.
(8) Pérez-Maqueda, L.; Criado, J. M.; Real, C.; Subrtb, J.; Bohácek, J. *J. Mater. Chem.* **1999**, *9*, 1839−1845.
(9) Froment, F.; Tournié, A.; Colomban, P. *J. Raman Spectrosc.* **2008**, *39*, 560−568.
(10) Legodi, M. A.; de Waal, D. *Dyes Pigm.* **2007**, *74*, 161−168.
(11) Cornell, R. M. and Schwertmann, U. *Iron Oxides in the Laboratory: Preparation and Characterization*; Wiley VCH: Weinheim, Germany, 2000.
(12) Nagano, T.; Nakashima, S.; Nakayama, S.; Senoo, M. *Clays Clay Miner.* **1994**, *42*, 226−234.
(13) Cornell, R. M.; Giovanoli, R. *Clays Clay Miner.* **1986**, *34*, 557−564.
(14) Cornell, M.; Giovanoli, R. *Clays Clay Miner.* **1985**, *33*, 424−432.
(15) Lewis, D. G.; Schwertmann, U. *J. Colloid Interface Sci.* **1980**, *78*, 543−553.
(16) Popov, V. V.; Gorbunov, A. I. *Russ. J. Inorg. Chem.* **2010**, *55*, 1508−1514.
(17) Gilbert, F.; Refait, P.; Leveque, F.; Remazeilles, C.; Conforto, E. *J. Phys. Chem. Solids* **2008**, *69*, 2124−2130.
(18) O'Connor, D. L.; Dudukovic, M. P.; Ramachandran, P. A. *Ind. Eng. Chem. Res.* **1992**, *31*, 2516−2524.
(19) Kiyama, M.; Shamoto, S.; Holman, N.; Okuda, Y.; Takada, T. *Bull. Inst. Chem. Res. Kyoto Univ.* **1986**, *64*, 150−156.
(20) Olowe, A. A.; Génin, M. R. *Corros. Sci.* **1991**, *32*, 965−984.
(21) Misawa, T.; Hashimoto, K.; Shimodaira, S. *Corros. Sci.* **1974**, *14*, 131−149.
(22) Génin, M. R.; Ruby, C.; Géhin, A.; Refait, P. *C. R. Geosci.* **2006**, *338*, 433−446.
(23) Domingo, C.; Rodríguez-Clemente, R.; Blesa, M. *J. Colloid Interface Sci.* **1994**, *165*, 244−252.
(24) Olowe, A. A.; Génin, M. R. *Corros. Sci.* **1991**, *32*, 1021−1028.
(25) Misawa, T.; Hashimoto, K.; Shimodaira, S. *J. Inorg. Nucl. Chem.* **1973**, *35*, 4167−4174.
(26) Olowe, A. A.; Refait, P.; Génin, M. R. *Corros. Sci.* **1991**, *32*, 1003−1020.
(27) Tamaura, Y.; Buduan, P. V.; Katsura, T. *J. C. S. Dalton* **1981**, 1807−1811.
(28) Ristic, M.; Opacak, I.; Music, S. *J. Alloys Compd.* **2013**, *559*, 49−56.
(29) Fu, D.; Keech, P. G.; Sunb, X.; Wren, J. C. *Phys. Chem. Chem. Phys.* **2011**, *13*, 18523−18529.
(30) Shavel, A.; Liz-Marzán, L. M. *Phys. Chem. Chem. Phys.* **2009**, *11*, 3762−3766.
(31) Thies-Weesie, D. M. E.; de Hoog, J. P.; Hernandez Mendiola, M.; Petukhov, A. V.; Vroege, G. J. *Chem. Mater.* **2007**, *19*, 5538−5546.
(32) Yu, T.; Park, J.; Moon, J.; An, K.; Piao, Y.; Hyeon, T. *J. Am. Chem. Soc.* **2007**, *129*, 14558−14559.
(33) Liang, X.; Wang, X.; Zhuang, J.; Chen, Y.; Wang, D.; Li, Y. *Adv. Funct. Mater.* **2006**, *16*, 1805−1813.
(34) Sudakar, C.; Nagarajarao, G.; NarayananKutty, T. R. *J. Mater. Chem.* **2002**, *12*, 107−116.
(35) Frini, A.; El Maaoui, M. *J. Colloid Interface Sci.* **1997**, *190*, 269−277.
(36) Carlson, L.; Schwertmann, U. *Clay Miner.* **1990**, *25*, 65−71.
(37) Kumazawa, H.; Kawasaki, H.; Ikeda, N. *Chem. Eng. Commun.* **2000**, *179*, 81−88.
(38) Wang, T.; Jin, Y.; Wang, Z.; Yu, Z. *Chem. Eng. J.* **1998**, *69*, 1−5.
(39) Sato, T.; Okamoto, S.; Hashimoto, K. J. *Ceram. Soc. Jpn.* **1986**, *94*, 1201−1205.
(40) Kiyama, M. *Bull. Chem. Soc. Jpn.* **1974**, *47*, 1646−1650.
(41) Lau, O. W. *J. Chem. Educ.* **1979**, *56*, 474.
(42) Bernal, J. D.; Dasgupta, D. R.; Mackay, A. L. *Clay Miner. Bull.* **1959**, *4*, 15−30.
(43) Oh, S. J.; Cook, D. C.; Townsend, H. E. *Hyperfine Interact.* **1998**, *112*, 59−65.
(44) Hanesch, M. *Geophys. J. Int.* **2009**, *177*, 941−948.
(45) Frost, R. L.; López, A.; Scholz, R.; Xi, Y.; da Silveira, A. J.; Fernandes Lima, R. M. *Spectrochim. Acta, Part A* **2013**, *114*, 85−91.
(46) Schwertmann, U.; Cambier, P.; Murad, E. *Clays Clay Miner.* **1985**, *33*, 369−378.
(47) Mersmann, A. *Crystallization Technology Handbook*, 2nd ed.; Marcel Dekker: New York, 2000.
(48) Sherman, D. M.; Waite, T. D. *Am. Mineral.* **1985**, *70*, 1262−1269.
(49) Zhang, H.; Bayne, M.; Fernando, S.; Legg, B.; Zhu, M.; Penn, R. L.; Banfield, J. F. *J. Phys. Chem. C* **2011**, *115*, 17704−17710.
(50) Chernyshova, I. V.; Ponnurangam, S.; Somasundaran, P. *Phys. Chem. Chem. Phys.* **2010**, *12*, 14045−14056.
(51) Lutz, H. D.; Möller, H.; Schmidt, M. *J. Mol. Struct.* **1994**, *328*, 121−132.
(52) Francombe, M. H.; Rooksby, H. P. *Clay Miner. Bull.* **1959**, *4*, 1−14.
(53) Okamoto, S. *J. Am. Ceram. Soc.* **1968**, *51*, 594−599.
(54) Tromans, D. *Ind. Eng. Chem. Res.* **2000**, *39*, 805−812.
(55) Zhang, C.; Fan, F. R.; Bard, A. J. *J. Am. Chem. Soc.* **2009**, *131*, 177−181.
(56) Chen, P.; Xu, K.; Li, X.; Guo, Y.; Zhou, D.; Zhao, J.; Wu, X.; Wu, C.; Xie, Y. *Chem. Sci.* **2014**, *5*, 2251−2255.
(57) Jolivet, J. P.; Chanéac, C.; Tronc, E. *Chem. Commun.* **2004**, 481−487.
(58) Blesa, M.; Matijevic, E. *Adv. Colloid Interface Sci.* **1989**, *29*, 173−221.
(59) Vu, T. A.; Reagan, M. M.; Li, D.; Legg, B.; De Yoreo, J. J.; Banfield, J. F.; Zhang, H. *CrystEngComm* **2014**, *16*, 1466−1471.
(60) Varanda, L. C.; Morales, M. P.; Jafelicci, M.; Serna, J. C. *Mater. Chem.* **2002**, *12*, 3649−3653.
(61) Silvester, E.; Charlet, L.; Tournassat, C.; Géhin, A.; Greneche, J.; Liger, E. *Geochim. Cosmochim. Acta* **2005**, *69*, 4801−4815.
(62) Hiemstra, T.; van Riemsdijk, W. H. *Geochim. Cosmochim. Acta* **2007**, *71*, 5913−5933.
(63) Stumm, W. *Croat. Chem. Acta* **1997**, *70*, 71−93.
(64) Sung, W.; Morgan, J. J. *Environ. Sci. Technol.* **1980**, *14*, 561−568.
(65) (a) Tamura, H.; Goto, K.; Nagayama, M. *Corros. Sci.* **1976**, *16*, 197−207. (b) Tamura, H.; Kawamura, S.; Hagayama, M. *Corros. Sci.* **1980**, *20*, 963−971.
(66) Russell, B.; Payne, M.; Colombi Ciacchi, L. *Phys. Rev. B* **2009**, *79*, No. 165101.
(67) Millero, F. *Geochim. Cosmochim. Acta* **1985**, *49*, 547−553.
(68) Morgan, B.; Lahav, O. *Chemosphere* **2007**, *68*, 2080−2084.
(69) Olowe, A. A.; Génin, M. R. *Hyperfine Interact.* **1991**, *69*, 823−826.